Controlled Anisotropic Wetting by Plasma Treatment for Directed Self-Assembly of High-χ Block Copolymers

Achmad Fajar Putranto, Camille Petit-Etienne, Sébastien Cavalaglio, Benjamin Cabannes-Boué, Marie Panabiere, Gianluca Forcina, Guillaume Fleury, Martin Kogelschatz, Marc Zelsmann

Controlled anisotropic wetting by plasma treatment for directed self-assembly of high-χ block copolymers

Achmad Fajar Putranto,*,† Camille Petit-Etienne,† Sébastien Cavalaglio,†

Benjamin Cabannes-Boué,‡ Marie Panabiere,† Gianluca Forcina,† Guillaume

Fleury,‡ Martin Kogelschatz,† and Marc Zelsmann*,†

†*Université Grenoble Alpes, CNRS, CEA/LETI Minatec, Laboratoire des Technologies de la Microélectronique (LTM), 38000, Grenoble, France*

‡*Univ. Bordeaux, CNRS, Bordeaux INP, LCPO, UMR 5629, F-33600, Pessac, France*

E-mail: fajarputranto6@gmail.com; marc.zelsmann@cea.fr

Phone: (+33) 438789292. Fax: (+33) 438785892

Abstract

The directed self-assembly (DSA) of block copolymers (BCPs) is a promising next-generation lithography technique for high-resolution patterning. However, achieving lithographically applicable BCP organization such as out-of-plane lamellae requires a proper tuning of interfacial energies between the BCP domains and the substrate that remains difficult to address effectively and efficiently with high-χ BCPs. Here, we present the successful generation of anisotropic wetting by plasma treatment on patterned spin-on-carbon (SOC) substrates and its application to the DSA of a high-χ Si-containing material, poly(1,1-dimethylsilacyclobutane)-*block*-polystyrene (PDMSB-*b*-PS), with a 9 nm half pitch. Exposing the SOC substrate to different plasma chemistries promotes the vertical alignment of the PDMSB-*b*-PS lamellae within trenches. In particular, a patterned substrate treated with HBr/O_2 plasma gives both a neutral wetting at the bottom interface and a strong PS-affine wetting at the sidewalls of the SOC trenches to efficiently guide the vertical BCP lamellae. Furthermore, prolonged exposure to HBr/O_2 plasma enables an adjustment of the trench width and/or an increased density of BCP lines on the substrate. Experimental observations are in agreement with a free energy configurational model developed to describe the system. These advances, which could be easily implemented in industry, could contribute to the wider adoption

of self-assembly techniques in microelectronics, and beyond to applications such as metasurfaces, surface-enhanced Raman spectroscopy, and sensing technologies.

Keywords: *anisotropic wetting, directed self-assembly, block copolymer lithography, graphoepitaxy, plasma etching, nanopatterning*

TOC graphic:

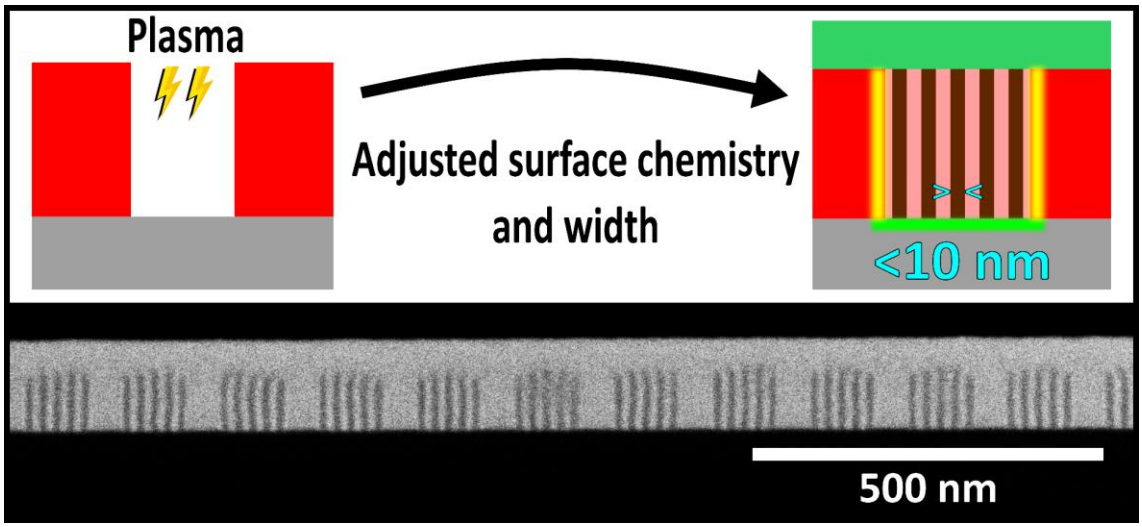

INTRODUCTION

Over the past decade, the scaling of nanofeatures has progressed to the sub-10 nm scale, primarily driven by the microelectronics industry's quest for continual enhancements in device performance.[1–4] The drive towards sub-10 nm features is important for maintaining the trajectory of device miniaturization, which is essential for improving performance, power efficiency, and packing density in integrated circuits.[5] Nevertheless, sub-10 nm resolutions are still challenging, as current high resolution top-down techniques like electron beam and extreme ultraviolet lithography (EBL and EUVL, respectively) are hampered by cost and efficiency issues.[6–8] Overcoming these hurdles requires innovative solutions, which has led to interest in bottom-up methods like block copolymer (BCP) lithography.[9] BCP lithography relies on microphase

separation of chemically distinct blocks, resulting in diverse morphologies like lamellae, spheres, and cylinders by adjusting the BCP composition.[10]

To achieve sub-10 nm feature manufacturing, it is necessary to use BCPs with a high χ value where χ, the Flory-Huggins parameter, represents the incompatibility between the blocks. In the context of lithographically applicable BCP organizations, such as the out-of-plane lamellar structure, it is common practice to confine the high-χ BCP layer between underlayer (UL) and top coat (TC) materials. This arrangement aimed at achieving a balance in interfacial energy between each BCP domain and the top and bottom interfaces to favor a vertical alignment.[11–15] Although some studies have successfully reported the synthesis of high-χ materials with closely matched surface energies,[16–19] thereby effectively avoiding the need for a TC layer, sequential infiltration synthesis (SIS) had to be used in these cases to overcome the lack of chemical selectivity. Indeed, another crucial factor in BCP lithography is the need for etch selectivity between blocks. Apart from SIS, this can be more easily achieved using BCPs with a Si-containing block. Then, a very elegant way to produce neutral topcoats was demonstrated in a study by Oh et.al.[20] where a filtered Ar plasma is used to crosslink directly the surface of the BCP to create such TC. Nevertheless, the TC is then not completely organic, which can bring some issues during the plasma transfer etching of the features, and do not allow an additional control over the thin film stability due to its very small thickness. Actually, thin films of high resolution polymers are easily prone to dewet[15] and we have demonstrated that a thicker and rigid TC is able to overcome these instabilities.[12] Finally, it has to be noted that the use of an organic TC is not a problem for the transfer of Si-containing perpendicularly oriented lamellae into underlying substrates (spin-on-carbon (SOC), SiN, and Si).[11,21]

Achieving long-range order in BCP structures necessitates directed self-assembly (DSA), utilizing topographical or chemically modified surfaces - known as graphoepitaxy or chemoepitaxy respectively.[22,23] On one hand, chemoepitaxy relies on very high-resolution chemical templates generated through intricate multistep lithographic processes, to produce dense line arrays with sub-10 nm resolution.[14,17,18,24,25] On the other hand, the less finely resolved topographic

substrates necessary for graphoepitaxy can be efficiently manufactured using well-established fabrication techniques, such as 193 nm photolithography.[25,26] Nevertheless, the use of topographic patterns to direct BCP self-assembly comes with a significant limitation, namely the control of the interfacial interactions between the patterned template and the BCP domains (particularly with regard to the sidewalls of the guiding lines). Indeed, it is important to achieve neutral wetting at the top and bottom interfaces, while it is equally crucial to establish sufficient preferential interaction on the sidewalls to facilitate the long-range order and the formation of vertically oriented lamellae into the topographic trenches. Accordingly, the establishment of a chemical contrast between the bottom and lateral surfaces is of paramount importance for DSA implementation by graphoepitaxy. The deposition of an UL over the patterned substrate before BCP deposition results in general in a uniform interfacial interaction at the bottom and lateral surfaces, which is not thermodynamically favorable to the formation of long-range order lamellae along the guiding structures. Park and coworkers[22] successfully generated a chemical contrast between the sidewalls and bottom surface by integrating both chemical and topographic patterning methods, employing a grafting layer and Au guidelines respectively, prior to the self-assembly of the BCP. However, it is important to consider the non-industrially compatible and complex processes involved in fabricating anisotropic wetting substrate and that the BCP employed in this work is not a high-χ BCP (PS-*b*-PMMA). Additionally, Lane and coll.[27] presented an approach that combines brush layer grafting with pattern trimming through O_2 plasma for DSA on topographic substrate, establishing chemical contrast between the substrate and resist guiding lines formed via nanoimprint lithography (NIL). Although the later approach effectively applied this method to guide the assembly of high-χ BCP chains into vertically aligned lamellae, it is noteworthy that they observed a reduction in the chemical contrast between the NIL lines and the substrate, as the brush grafts to both surfaces.

Here, we demonstrate the successful generation of anisotropic wetting by plasma treatment on a patterned substrate and applied this technique to the DSA of a Si-containing high-χ material, poly(1,1-dimethylsilacyclobutane)-*block*-polystyrene (PDMSB-*b*-PS),[28] with a 9 nm half pitch. We

employed photolithography-based graphoepitaxy substrates that consists of an industrially compatible material for guiding lines, *i.e.*, SOC. A set of plasma treatments were performed to investigate the surface energy modifications of the topographical templates (SOC sidewalls and Si bottom interface), thereby tuning their surface interactions with the PDMSB-*b*-PS domains. Subsequently, a sequence of plasma etching processes was employed to open the BCP mask. Our work therefore demonstrates a novel industry-compatible approach to generate anisotropic surface wetting and its application to achieving sub-10 nm nanoscale patterning using DSA, and provides a glimpse of the technique's potential for advanced semiconductor fabrication.

RESULTS AND DISCUSSIONS

Modification of the wetting of SOC lines by plasma treatments

For the implementation of the DSA of sub-10 nm half-pitch lamellar BCP chains, SOC lines were obtained from a tri-layer photolithography stack commonly used in the microelectronic industry (composed of resist lines, silicon anti reflective coating (SiARC) and SOC on Si substrate) using dedicated plasma etching processes (Fig. S1). The SOC insolubility in common organic solvents enabled the spin-coating of a PDMSB-*b*-PS solution onto the substrate featuring the SOC guiding lines (120 nm height and 95 nm wide trenches). In order to neutralize the wetting interaction at the top interface, a TC layer was deposited and crosslinked before the self-organization thermal annealing. However, although this TC chemistry has been demonstrated neutral towards lamellar PDMSB-*b*-PS BCPs on brush modified Si surface,[12] its effectiveness to drive the vertical orientation of lamellae into patterned SOC lines remains insufficient since a horizontal orientation was observed by default (Fig. 1). This suggests that the Si substrate is not sufficiently neutral with respect to the sidewalls. We believe the observed arc-shape structure of the lamellae comes from the fact that the TC/BCP interface is not perfectly horizontal but curved, even during self-assembly annealing. Indeed, this curved interface appears due to wetting of the BCP and TC solutions during the spin-coating fabrication steps and is then fixed when the TC is crosslinked before the self-assembly step. Since this configuration destabilizes more the horizontal configuration (energetic penalty of the bended lamellae) than the desired and targeted vertical one, we considered in the following discussions that the top interface of the BCP is horizontal. Finally, to generate a lithography-compatible pattern, it is then essential to precisely and independently adjust the BCP interactions with both the substrate and sidewalls. In this study, plasma processes, commonly employed in the industry, were selected to modify the wetting interactions of the Si substrate and the organic SOC sidewalls with respect to the PS and PDMSB domains.

Plasmas provide an effective means of modifying surface energies. The interaction of a mixture of ions, electrons, neutrals, and radicals from the plasmas with the surface enables surface chemical changes, which accordingly modify the surface energies.[29–31] In this work, F- and O_2-based plasmas were evaluated for the modification of the surface properties of Si and SOC substrates, rendering the surfaces hydrophobic and hydrophilic respectively.[32] Furthermore, the HBr/O_2 chemistry was also investigated as it is commonly used for resist line trimming and smoothing processes in lithography[33,34] (detailed parameters of the plasmas can be found in Table S1). In addition to that, to see the influence of the plasma on the chemical composition of the sidewalls, XPS measurements were performed on a planar SOC (post wet HF 10s) before and after 5s HBr/O_2 plasma treatment (the results are shown Fig. S3).

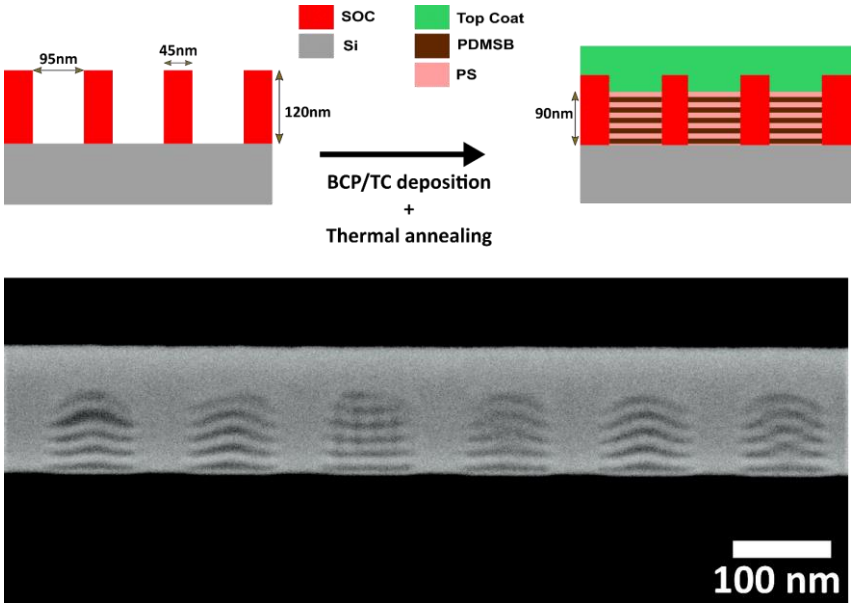

Figure 1. PDMSB-*b*-PS in-plane lamellar morphology with 18 nm periodicity spun into SOC trenches with a 1.14 aspect ratio, confined by a neutral TC layer. The stack underwent sequential thermal annealing for TC crosslinking and promotion of the self-assembly for 10 min at 90 °C and 10 min at 120 °C, respectively.

To assess the changes of surface energy following the various plasma treatments, contact angle measurements were performed on equivalent flat samples. Each specimen was obtained from a similar initial trilayer stack of the periodic SOC lines substrate. The main difference is the

complete removal of the photoresist mask at the start of the process by rinsing with a solvent to obtain non-patterned, large-area samples. Beyond this distinction, the remaining steps followed similar procedures. Since non-biased plasma are used for surface modifications, it is supposed that horizontal SOC surfaces are modified in the same way as vertical SOC sidewalls when treating patterned substrates. Further information regarding these processes can be found in Fig. S2. The contact angles of three liquids (water, ethylene glycol and glycerol) were recorded on the Si and SOC surfaces (at least five measurements for each liquid). From the measured contact angles, the polar and dispersive surface energy components, represented as γ^P and γ^D respectively, were subsequently assessed employing Owens, Wendt, Rabel, and Kaelble (OWRK) method.[35] From these surface energies and the ones of PS and PDMSB retrieved from literature,[25] interfacial tensions of the individual BCP domains on Si and SOC surfaces were determined using Wu equation.[36]

The influence of each plasma treatment on creating contrasting wetting properties at the bottom and lateral surfaces can be examined by observing changes in lamellar configurations. It was first investigated by introducing the measured surface tensions into a free energy configurational model. At thermodynamic equilibrium, the most favored lamellar orientation must possess the lowest energy configuration. Turner[37] and Walton[38] proposed a model for the free energy E of a symmetric BCP thin film confined between two horizontal infinite plates as follows:

$$E = k_B T \frac{3p}{8N\alpha^2} L^2 + \frac{2pN\alpha^3}{L} \gamma_{A/B} + 2E_S \quad (1)$$

where $k_B, p, N, \alpha, \gamma_{A/B}$ and L stand for Boltzmann constant, number of copolymer chains in the system, degree of polymerization, statistical segment length, interfacial tension between the A and B blocks of the BCP and lamellar periodicity of the BCP, respectively. The first two terms describe the volume interactions: the free energy related to the elastic stretching of the polymer chains, and the free energy related to the creation of A-B interfaces in the polymer. The minimal value of these two terms in bulk is obtained for $L = L_0$, the equilibrium bulk lamellar periodicity.

In thin films, the minimization of these volume terms then describes the commensurability of the layer thickness D with L_0 in the case of horizontally-oriented lamellae. The last term, E_S, represents the interaction between the BCP and the top/bottom surfaces that depends on the lamellar configuration, *i.e.*, horizontal symmetric, horizontal asymmetric, or vertical. In other words, the minimization of $E(L)$ enables to investigate the effect of commensurability of the layer thickness as well as the relative effect of volume and surface contributions.

The above model describes an infinite planar system. In our case, to take into account interactions with trench sidewalls, an additional term must be added and three possible general lamellae orientations have to be considered: horizontal, vertical and ladder structures (Fig. S4), depending on the wetting interaction between the BCP domains and the surfaces. Supposing a perfectly neutral TC, anisotropic wetting between the bottom surface and the sidewalls favors either a horizontal or vertical orientation of lamellar BCPs. On the other hand, if isotropic interactions are present, a ladder structure is preferred (Fig. S5). As detailed below, a neutrality level for the BCP can be determined for any surface as the absolute difference in interfacial tensions of each block with this surface. Since we aim for a certain dissimilarity in the neutrality level between the Si substrate and the SOC sidewalls through selected plasma treatments, the ladder structure is never the most favorable configuration in our experiments as will be further discussed later. Therefore, the following discussion focuses solely on the comparison between vertical and horizontal orientations. Recognizing that a vertical configuration is analogous to a horizontal configuration rotated by 90° and considering the distinct areas of the various interfaces, Eq. 1 can be modified to describe the free energy per unit area, F_j, of the polymer system in trenches in all possible vertical or horizontal configurations:

$$F_j = a_j \left(\frac{{b_j}^3}{m^2} \gamma_{A/B} + 2m \gamma_{A/B} + 2F_S \right) + 2b_j F_{side} \quad (2)$$

where $j = H$(horizontal) or V(vertical),

- if $j = H$, $a_j = w$, $b_j = d$, S = TC / Si and side = SOC
- if $j = V$, $a_j = d$, $b_j = w$, S = SOC and side = TC / Si

$d = D/L_0$ is the normalized film thickness, $w = W/L_0$ is the normalized trench width, m represents the number of lamellae that are fitted either laterally into the trench (vertically oriented lamellae) or in the BCP height (horizontally oriented lamellae), $m = n$ for a symmetric wetting case whereas $m = n + 1/2$ for an asymmetric case (n is an integer used for the calculation to evaluate the free energy of all configuration with all possible lamella numbers) and F_j in the units of surface tensions (mN/m). The details of the derivation from Eq. 1 to Eq. 2 are provided in the supporting information file.

The free energy of each configuration for the various plasma-treated substrates can then be calculated. The A-B block interfacial energy $\gamma_{A/B} = (k_B T/\alpha^2)\sqrt{\chi/6}$ is dependent on χ and α. Using $\chi_{PDMSB/PS} = 0.07$ and the statistical segment length average of PDMSB[28] and PS[39] $\alpha_{PDMSB/PS} = 0.89$ nm, it resulted in $\gamma_{A/B} = 0.56$ mN/m. Since the used top-coat had been proven to be neutral in a previous study,[12] we assumed a perfectly neutral top coat for modelling. The complete descriptions of Eq. 2 including F_S and F_{side}, and interfacial tension values between PDMSB/PS blocks and surfaces are given in Table S2 and S3.

To evaluate the preferred lamellar orientation, we finally plotted the difference in the BCP free energies between the most favorable (minimal) vertical and horizontal configurations ($F_{V-min} - F_{H-min}$) at given (experimental) normalized BCP thicknesses d ($d_{ref} = 5.7$, $d_{CHF3} = 5.7$, $d_{O_2} = 5.2$, $d_{HBr/O_2} = 5.4$ obtained from scanning transmission electron microscopy (STEM) images) with respect to the normalized trench width w (Fig. 2). If the subtraction ($F_{V-min} - F_{H-min}$) yields a positive value, a horizontal orientation is favored; conversely, if the result is negative, a vertical orientation is preferred.

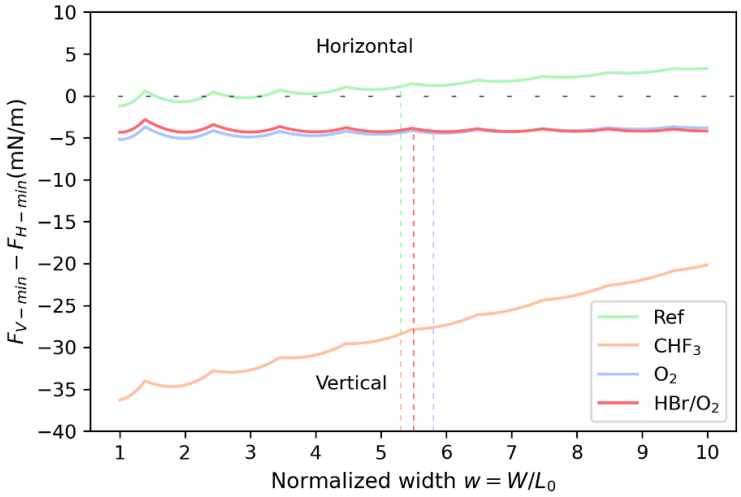

Figure 2. Differences in PDMSB-*b*-PS thin-film free energies in a SOC trench between the most favorable vertical and horizontal configurations ($F_{V-min} - F_{H-min}$) pre- and -post plasma treatments as a function of normalized trench width (w). For a given *w*, if the value of ($F_{V-min} - F_{H-min}$) is positive, a horizontal orientation is preferred; if it is negative, a vertical configuration is favoured. The vertical dashed lines indicate the corresponding experimental w.

From this modelling, the initial observation is that the influence of commensurability (the "corrugation" of the curves) diminishes after a few units of w compared to the contributions from surface tensions. Additionally, among all treated surfaces, the CHF_3-treated substrate stands out as the most energetically favorable case for vertical orientation. Moreover, for the reference case (untreated substrate), a horizontal configuration is predicted for nearly all trench widths, while vertical configurations are anticipated for all plasma-treated surfaces. In particular, at the trench widths corresponding to the experimental conditions extracted from STEM ($w_{Ref} = 5.3, w_{CHF3} = 5.3, w_{O2} = 5.8, w_{HBr/O_2} = 5.5$, as highlighted by the vertical dashed lines in Fig. 2), the initial horizontal orientation (as illustrated in Fig. 1 and corresponding to “Ref” in Fig. 2) is expected to transform into vertically oriented lamellae after plasma treatments. This aligns with experimental observations made by STEM (see Fig. 3), as a vertical organization of the lamellae is observed for all plasma treated substrates. Considering the possibility of a ladder structure observation (corresponding configurational free energy equation given in Table S2), we thus verified that it is indeed always the least favorable case for any substrate (Fig. S6).

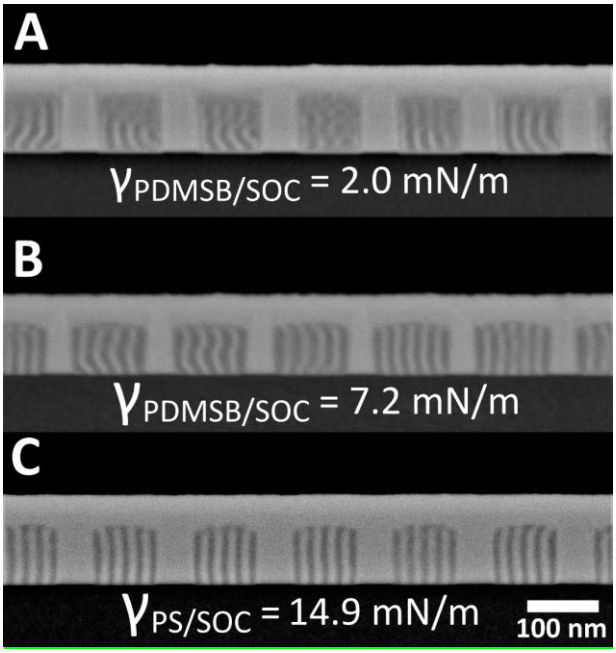

Figure 3. Cross-sectional STEM images highlighting the orientation of PDMSB-*b*-PS lamellae confined between SOC trenches with respect to various plasma treatments: A. CHF_3, B. O_2, and C. HBr/O_2. The quality of vertical extension (wobbling of lamellae) observed is directly linked to the interfacial tension between by the BCP domains wetting the SOC sidewalls ($\gamma_{i/SOC}$). The promotion of the self-assembly was performed at 120 °C for 10 min for all samples.

As w increases, or similarly as the SOC lines height decreases, the influence of the sidewalls becomes less significant. A constant increase of the ($F_{V-min} - F_{H-min}$) value for the CHF_3- and O_2-treated substrates with w predicts that an orientation transition of PDMSB-*b*-PS lamellae from vertical to horizontal will occur at a certain trench width (i.e., $w_{CHF3} > 21$ and $w_{O2} > 34$) as depicted in Fig. S7. However, the lamellar orientation on HBr/O_2-treated substrates appear to be independent on w. This is due to the almost perfect neutrality level obtained with this plasma at the Si bottom surface. The neutrality level can be determined by the absolute difference in interfacial energy $\Delta(\gamma_i)$ between PS and PDMSB on i = Si or SOC surfaces ($\Delta(\gamma_i)$ values are reported in Fig. 4, surface energy values are shown in Table S3). A perfectly neutral interaction is represented by a value of $\Delta(\gamma_i)$ = 0 (both BCP blocks wet the surface with an equally high interfacial tension), and as the absolute value of $\Delta(\gamma_i)$ increases, the wetting interaction becomes progressively preferential to one block. As a result, preferential surfaces are likely to be wetted

predominantly by one of the BCP block, while neutral surfaces interact indifferently with PS and PDMSB blocks. The neutrality level $\Delta(\gamma_i)$ of PDMSB-*b*-PS on HBr/O_2 treated Si is very small ($\Delta(\gamma_{Si}) = 0.04$ mN/m), retaining the lamellae verticality over w. This effect was already shown in another study[40] in which, with the supposedly perfect neutral top coat and neutral bottom interface, the minimum value of the difference between vertical and horizontal orientation is constant with the normalized thickness d.

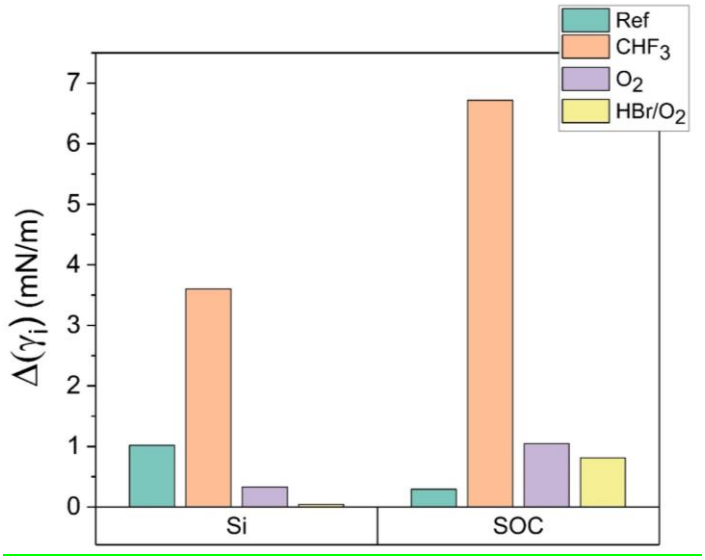

Figure 4. Absolute difference in interfacial energy between PS and PDMSB with respect to Si and SOC surfaces ($\Delta(\gamma_i) = \left|\gamma_{PS/i} - \gamma_{PDMSB/i}\right|$ where *i* = Si, SOC) assessed both before and after a 5-second plasma treatment. The values of $\gamma_{PS/i}$ and $\gamma_{PDMSB/i}$ were determined using Wu's equation,[36] taking into account the corresponding surface energies of Si and SOC, as well as with the PS and PDMSB surface energy values obtained from literature.[25]

Since the effect of commensurability is low in our system compared to surface tension effects, the observed lamellae orientations can be more comprehensively explained by an inversion in the neutrality level between the Si surface and SOC sidewalls. The resulting BCP structure is mostly determined by a "competition" resulting from interactions on each surface - top, bottom and the two lateral sides. Fig. 4 shows indeed that before plasma treatment, the interfacial energy difference between PS and PDMSB with Si is higher than that with SOC ($\Delta(\gamma_{Si}) > \Delta(\gamma_{SOC})$), leading

to in-plane lamellae as observed experimentally. On the other hand, after plasma treatment, all treated samples are characterized by $\Delta(\gamma_{Si}) < \Delta(\gamma_{SOC})$: a vertical organization is expected.

Another very important aspect in this study is the disparity that exists in the manner of which BCP domains (PS or PDMSB) wets the sidewalls of the substrate. First, it is predicted (and observed experimentally, as detailed more clearly in Fig. S8) that it is the PDMSB block that wets the SOC sidewalls in the case of CHF_3 and O_2 plasma-treated samples, whereas it is the PS block in the case of HBr/O_2 plasma. Second, we observe that the magnitude of the interfacial tensions of the block that is wetting seems to play a crucial role to direct efficiently the BCP structure along the guiding lines. On Fig. 3A, the notably curved vertical lamellae formed at $\gamma_{PDMSB/SOC} = 2.0$ mN/m indicates a poor guiding strength in the case of the fluorinated-treated substrate. Lamellae began to demonstrate a more satisfactorily straight configuration at $\gamma_{PDMSB/SOC} = 7.2$ mN/m (pure oxygen treated surfaces, Fig. 3B) but best organization quality seems to appear for $\gamma_{PS/SOC} = 14.9$ mN/m, and this outcome was achieved through modification of the substrate using HBr/O_2 treatment (Fig. 3C). These results imply that the quality of the perpendicular lamellae directly correlates with the interfacial tension of the BCP domain that is wetting the SOC sidewalls, which is also observed in the literature.[41,42] Some might argue that the perpendicularity of the lines is affected by the commensurability between the BCP periodicity and the width of the trenches. However, as shown in Fig. 2, within the corresponding normalized trench width of CHF_3, HBr/O_2, and O_2 plasma-treated substrates (i.e., $5 < w < 6$), the corrugation of the curve is small and hence, the commensurability effect is minimum. Therefore, the level of surface tension of the wetting block to the sidewalls is an important driving force to achieve a robust out-of-plane lamellae organization.

Finally, we can define an "affinity ratio" $\Delta(\gamma_{SOC})/\Delta(\gamma_{Si})$ with respect to the BCP wetting on Si and SOC surfaces. It varies from 0.29 in the initial state, to 1.86, 3.13 and 18.78 after surface treatments using CHF_3, O_2, and HBr/O_2 plasmas, respectively. The $\Delta(\gamma_{SOC})/\Delta(\gamma_{Si})$ ratio allows us to draw the two following conclusions: i. The configuration favorability; *i.e.,* $\Delta(\gamma_{SOC})/\Delta(\gamma_{Si}) < 1$ indicates a preference for a horizontal lamellar orientation. Conversely, $\Delta(\gamma_{SOC})/\Delta(\gamma_{Si}) > 1$ suggests

a vertical alignment of the lamellae; and ii. The quality of vertical alignment is correlated to the $\Delta(\gamma_{SOC})/\Delta(\gamma_{Si})$ ratio. In other words, an increase in this ratio corresponds to an enhanced quality of vertical alignment.

Despite the challenges related to the generation of vertical lamellae with high-χ BCPs, the HBr/O_2 plasma treatment effectively established the desired chemical contrast between the SOC guiding lines and the Si substrate, leading to the vertical orientation of PDMSB-*b*-PS lamellae. Yet another advantage of this plasma treatment is the possibility to isotopically shrink (so-called plasma trimming) the SOC guiding lines, reducing both lateral and vertical dimensions. By doing so it is not only possible to fit more lamellae into the trenches, generating dense BCP line gratings on the surface, but it is also possible to adjust precisely the trench width to the natural bulk periodicity of the BCP. For example, by extending the HBr/O_2 plasma duration to 15s, it is possible to fit 7 PDMSB lamellae into the trenches (Fig. 5C) compared to the 5 lamellae of the 5s-treated sample (Fig. 5B). Even if the trimming process could be further optimized to produce even more vertical SOC sidewalls to reduce the defectivity, we believe it nevertheless demonstrates an additional control of the BCP behavior into the trenches by a single industry compatible plasma. This is an important progress in the domain of high-χ BCP DSA, offering the potential for efficient nanomanufacturing processes.

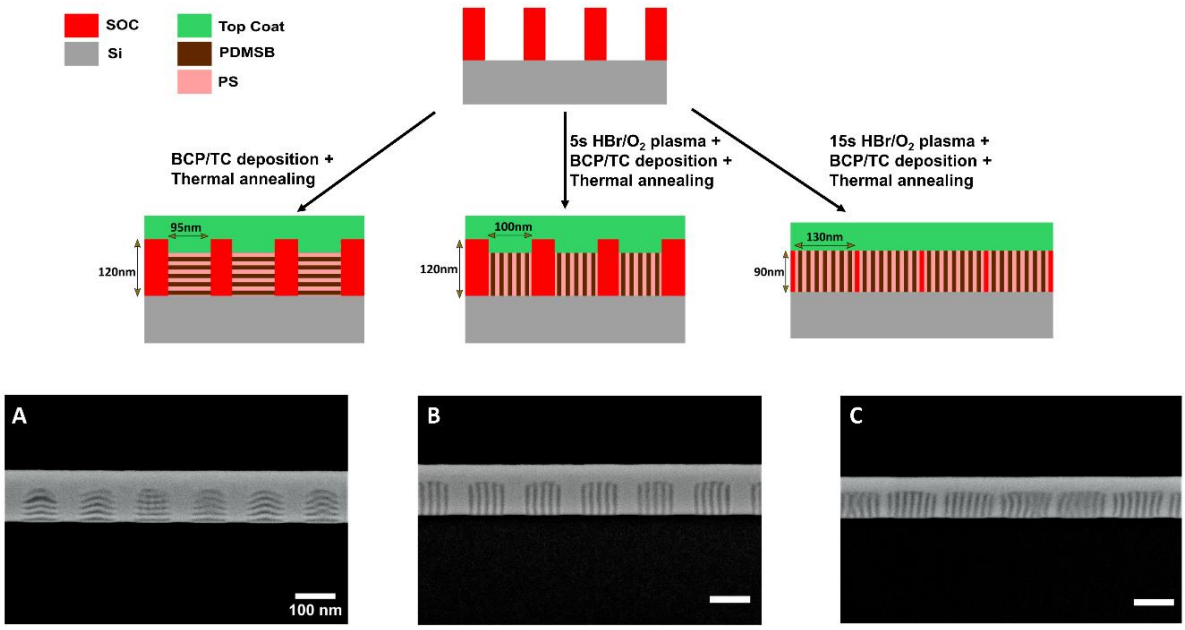

Figure 5. Impact of HBr/O_2 plasma on the DSA of PDMSB-*b*-PS organized into a graphoepitaxy substrate with SOC lines, confined by a TC: A. DSA at 120 °C for 10 min without any exposure to HBr/O_2 plasma. B. DSA at 120 °C for 10 min with a 5 s exposure to HBr/O_2 plasma on the SOC lines substrate. C. DSA at 240 °C for 5 min with a 15 s exposure to HBr/O_2 plasma on the SOC lines substrate.

Opening of PDMSB lines

A final objective is eventually to generate a PDMSB mask from the two variations of PDMSB-*b*-PS vertical lines organizations shown previously. This necessitates a series of dedicated plasma etching processes, outlined in Fig. 6. The initial step involves the removal of the TC using a H_2/N_2 plasma. This reducing plasma serves a dual function: eliminating the TC and curing the silicon-containing PDMSB block via the VUV radiation generated during the plasma process.[43,44] Relying on the Si-C bond in the PDMSB block, any O_2-based plasma should selectively etch PS and SOC with respect to PDMSB. However, the progressive increase in the relative Si composition compared to C during the oxidation process triggers the creation of an interfacial layer, *i.e.,* a thin

Si-containing layer, formed on top of the BCP that obstructs the etching process.[11] To counteract the creation of the thin Si layer, a fluorine-based plasma (CF_4/CHF_3) was introduced between the H_2-based plasma (H_2/N_2) and the O_2-based plasma ($He/N_2/O_2$) steps. Details of the plasma parameters used and processes are discussed in the supporting information (Table S1 and Fig. S9 respectively). All in all, by a combination of three different plasma gases (reducing, fluorine-based, and oxidizing), BCP thin films can be completely transformed into PDMSB lines masks, interspersed by 50 nm gaps, as depicted in Fig. 6A for the 5s-treated case, or with reduced gaps between PDMSB line clusters in the case of 15s-treated substrates, enabling the achievement of a consistent 9 nm half-pitch line array across the entire sample surface, as depicted in Fig. 6B. Finally, resulting PDMSB line patterns confirm that our approach to generate anisotropic wetting is compatible with high-χ BCPs and works with standard microelectronic etching processes. The mitigation of defects on the resulting lamellae was not a scope of this article and is currently being investigated in our group.

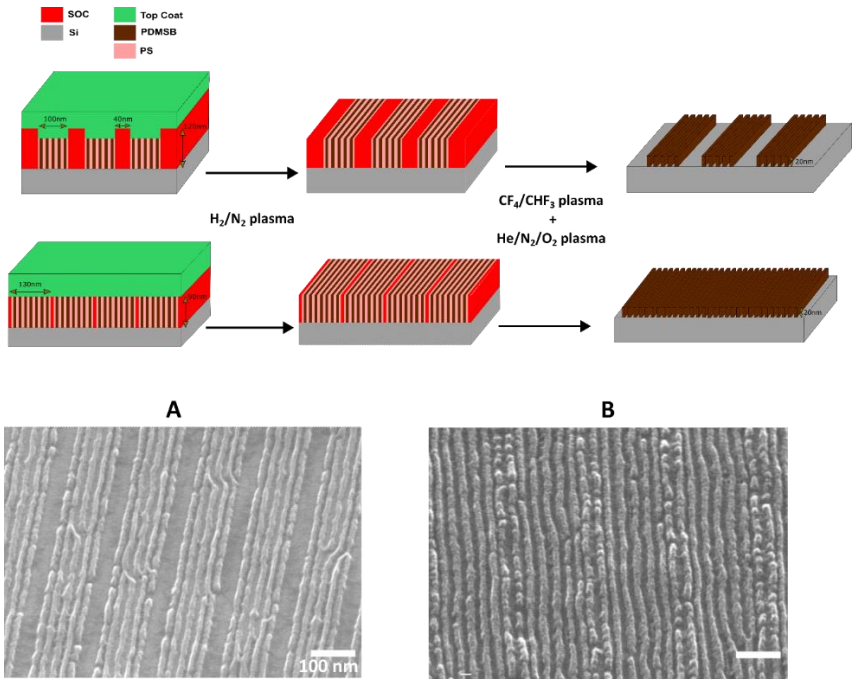

Figure 6. Revelation of PDMSB lines masks with varying densities and a resolution of 9 nm achieved using a combination of H_2/N_2, CF_4/CHF_3, and $He/N_2/O_2$ plasmas. Tilted-view SEM images

depict the resulting PDMSB lines: A. Featuring a 9 nm half-pitch interspersed by 50 nm gaps every 5 lines, and B. Exhibiting a consistent 9 nm half-pitch pattern across the entire surface.

CONCLUSIONS

In this study, we devised strategies compatible with the microelectronics industry to create line patterns with anisotropic wetting properties, effectively guiding the self-assembly of high-resolution BCPs. Utilizing SOC lines on silicon and employing 300 mm wafer-compatible equipment's, we demonstrated the approach using a 9 nm resolution silicon-containing lamellar PDMSB-*b*-PS BCP system. To achieve perpendicular PDMSB-*b*-PS lamellae, it was demonstrated that the affinity of the bottom surface must be more neutral for the copolymer than that of the sidewalls. Furthermore, the quality of the vertical orientation of BCP lines is found to be correlated to the amplitude of the interfacial tension between the SOC guiding lines and the BCP domain wetting the sidewalls. Upright perpendicular lines were successfully obtained with an unbiased HBr/O_2 plasma treatment. An additional advantage of this treatment is the precise control over trench width, allowing for commensurability with the block copolymer's intrinsic period or an increase in the number of lamellae. We believe that the developed processes extend beyond the microelectronics sector and encompasses applications like metasurfaces fabrication,[45,46] as well as advancements in areas like surface-enhanced Raman spectroscopy (SERS)[47] and sensing applications.[48,49] Another significant aspect of our research involved the utilization of a combination of reducing, fluorine-based, and oxidizing plasmas to effectively reveal the PDMSB mask, creating a mask for an eventual pattern transfer into the underlying substrate.

METHODS

Materials

Substrate

Trilayer stack of resist mask, silicon-anti-reflective-coating (SiARC) and spin-on-carbon (SOC) layers on 300 mm diameter wafers of [1,0,0]-oriented Si were prepared in the CEA-LETI cleanroom facilities. Through the utilization of dry and wet etching processes, the fabrication method yielded bulk structure of SOC and Si intended for contact angle experiment, and patterned SOC lines serving as graphoepitaxy substrates for the DSA process using high-χ BCP. The latter possessed dimensions of 120 nm in height and 45 nm in width for the lines, and a width of 95 nm for the trenches.

Block copolymer

This study used an 18 nm periodicity lamellar poly(1,1-dimethylsilacyclobutane)-*block*-polystyrene (PS-*b*-PDMSB) BCP at a concentration of 2 wt % in methyl isobutyl ketone (MIBK). More details of the macromolecular characteristics of this particular system can be found in the literature.[28]

Top coat

The top-coat (TC) solution was formulated from a statistical terpolymer of 2,2,2-trifluoro ethylmethacrylate, glycidylmethacrylate and 2-hydroxyl ethyl methacrylate and a thermal initiator (10 wt %) into a 7/3 ethanol/PGME mixture (3.5 wt % solution). More details of this TC can be found in the literature.[12]

The chemical structures of the BCP and TC can be found in Fig. S10.

Preparation of the polymer stack

The process starts with the spin coating of BCP and TC consecutively onto the SOC lines of the graphoepitaxy substrate. The subsequent step involves thermal annealing processes to cross link the TC and induce DSA of the BCP. The temperature set for cross-linking was 90 °C, which is slightly below the glass transition temperature (T_g) of the PS block in PDMSB-*b*-PS. Self-assembly was conducted at a temperature of 120 °C or 240 °C. The TC cross-linking and DSA steps had a duration of 5 minutes and 10 minutes.

Plasma etch

Reactor

Etching processes were conducted using a 300 mm AdvantEdge™ MESA™ Inductively Coupled Plasma (ICP) etching tool made by Applied Materials. The walls of the chamber were constructed with yttrium oxide. The plasma source consists of a dual-coil ICP with 13.56 MHz RF generators generating up to 3000 W of power. The electrostatic chuck had the ability to be polarized with bias power reaching a maximum of 1.5 kW. The reactor was equipped with the Pulsync™ RF system, allowing the source and bias power to be pulsed at various frequencies and duty cycles, ranging from a few tens of hertz to tens of kilohertz, and from a few percent to continuous wave plasma. The temperature of the carrier wafer was set at 60 °C, while the reactor body was maintained at 65 °C.

Chamber preparation

The samples (with dimension between 1×1 cm^2 and 2×2 cm^2) were affixed to 300 mm Si wafers using Kapton adhesive tape. The chamber conditioning process started with a set of cleaning steps performed without wafer: NF_3/Cl_2 plasma was used for 45 seconds, followed by Cl_2/O_2/Ar plasma for 45 seconds, and finally O_2 plasma for 30 seconds. For experiments involving H_2/N_2 plasma, the cleaning was followed by a 300-second conditioning plasma using H_2/N_2 on a blanket Si wafer. The

etching procedure using $He/N_2/O_2$ plasma BCP was performed after coating the chamber walls with carbon (CH_4 plasma for 40s). Following a process with carbon-coated walls, the chamber was routinely cleaned with O_2 plasma for 60 seconds.

Etch conditions

First of all, two type of plasmas, $Ar/CF_4/CH_3$ and HBr/O_2, were employed to open the SiARC then SOC trenches, respectively, from trilayer stack (Fig. S1). Then, it was followed by wet etching using HF 1 wt % to remove the remaining small amount of SiARC on SOC lines. Subsequently, in the context of BCP lithography, surface energy of the substrate was evaluated after three different nonbiased plasmas (*i.e.,* HBr/O_2, O_2, and CHF_3). Once the directed self-assembly of BCP was done, involved processes of plasma etching are in the following order: first, to remove the topcoat material by H_2/N_2, afterwards CF_4/CHF_3 was used to planarize the BCP and SOC height non-selectively while preventing the Si crust layer formation, then $He/N_2/O_2$ was performed to selectively eliminate the PS phase while preserving the PDMSB lamellae. The description of etching processes, type of plasmas used, and parameter values are described in Table S1.

Surface energy measurements and interfacial energy calculations

The contact angles of water, ethylene glycol, and glycerol on Si and SOC surfaces (five to eight measurements for each liquid) were measured using a Drop Shape Analyzer (DSA100, KRÜSS GmbH) in a cleanroom environment (23 °C, 45 % RH). The surface energy values of polar and dispersive components, denoted as γ^P and γ^D respectively, were evaluated using the Owens, Wendt, Rabel, and Kaelble (OWRK) approach.[35] These values were directly computed via the Advanced software provided by KRÜSS GmbH. Subsequently, interfacial tensions of the constituent blocks within the block copolymer (PS and PDMSB) on these surfaces were determined by employing Wu's equation.[36] The surface energies of both blocks of the BCP are set

from the literature[25] : PS = $43.5\ mN.m^{-1}$ = 42.1_{DISP} + $1.4_{POL}\ mN.m^{-1}$, PDMSB = $27.3\ mN.m^{-1}$ = 25.1_{DISP} + $2.2_{POL}\ mN.m_{-1}$.

Surface characterization

The tilted view and cross-sectional SEM images of nanostructures were acquired on a Hitachi S-5000 microscope at 30 kV electron acceleration voltage with 15 nA emission current. An Helios 450S-FEI dual beam microscope was used for sample preparation and STEM imaging of the sample at 25 kV. In the sample preparation stage, series of Pt protective layers were deposited on a 20 × 2 μm^2 surface area of the sample under an electron beam (3 kV, 3.2 nA, approximately 100 nm of Pt deposited) followed by a 600 nm thick Pt protective layer under a focused ion beam (30 kV, 0.43 nA). A 20 × 2 μm^2 specimen was then etched away from the substrate at a depth of approximately 4 μm, transferred to a grid via an Omniprobe needle for mechanical manipulation, and thinned under a focused ion beam (30 kV, decreasing emission current from 2.5 nA to 40 pA) to approximately 100 nm width. Transmission images of the cross section were finally recorded in the scanning mode at 29 kV and 100 pA on the same equipment using bright field detection.

X-ray Photoelectron Spectroscopy (XPS) measurement

Ex-situ x-ray photoelectron spectroscopy (XPS) analysis are conducted on a Theta 300™ spectrometer from ThermoFisher Scientific® with a monochromatic Al Kα x-ray source (hυ = 1486.6 eV) and a spot size of 400 µm is used. Peaks are de-convoluted using the Avantage™ software. For each element, the analysis consisted of five scans with a dwell time of 500 ms, a pass energy of 100 eV, and an energy step size of 0.1 eV.

Supporting Information

Detailed preparation of the patterned SOC lines substrate, plasma parameters used in this project, preparation of planar SOC and Si surfaces for contact angle measurement experiments, XPS surface chemistry analysis for a planar SOC surface before and after HBr/O_2 plasma treatment, illustration of the three possible general configurations of PDMSB-*b*-PS lamellar structure self-assembled in a SOC trench confined by a neutral TC layer, a SEM image of ladder structure obtained experimentally, detailed derivation of the free energy equation from Eq. 1 to Eq. 2, free energy equations of PDMSB-*b*-PS in a SOC trench confined by a neutral TC layer in any possible configurations, interfacial energy values of Si substrate and SOC sidewalls against PS/PDMSB block before and after different plasma treatments, free energy simulations of horizontal and vertical configurations compared to ladder structure in a SOC lines graphoepitaxy substrate, corresponding grey pixel values of the cross sectional areas of the BCP in Fig. 5, detailed etch processes and discussion of the PDMSB lines opening , and macromolecular architecture of the Si-containing PDMSB-*b*-PS.

Acknowledgement

This work was supported by the REX-7 project from Région Rhone Alpes and BPI France, by the French RENATECH network, by the ANR LabEx Minos n°ANR-10-LABX-55-01 and by the ANR project BONSAI n°ANR-21-CE09-0009.

References

(1) Lin, B. J. Making Lithography Work for the 7-Nm Node and beyond in Overlay Accuracy, Resolution, Defect, and Cost. *Microelectron. Eng.* **2015**, *143*, 91–101. https://doi.org/10.1016/j.mee.2015.04.033.

(2) Pan, Y.; Li, J.; Wang, W.; Ye, T.; Yin, H.; Huang, K.; Zhang, Z.; Zhang, Q.; Jia, K.; Wu, Z.; Luo, K.; Yu, J. Novel 10-Nm Gate Length MoS_2 Transistor Fabricated on Si Fin Substrate. *IEEE J. Electron Devices Soc.* **2019**, *7*, 483–488. https://doi.org/10.1109/JEDS.2019.2910271.

(3) Mohammed, M. U.; Nizam, A.; Ali, L.; Chowdhury, M. H. FinFET Based SRAMs in Sub-10nm Domain. *Microelectron. J.* **2021**, *114*, 105116. https://doi.org/10.1016/j.mejo.2021.105116.

(4) V., B. S.; Vadthiya, N. Design and Deep Insights into Sub-10 Nm Spacer Engineered Junctionless FinFET for Nanoscale Applications. *ECS J. Solid State Sci. Technol.* **2021**, *10* (1), 013008. https://doi.org/10.1149/2162-8777/abddd4.

(5) Cao, W.; Bu, H.; Vinet, M.; Cao, M.; Takagi, S.; Hwang, S.; Ghani, T.; Banerjee, K. The Future Transistors. *Nature* **2023**, *620* (7974), 501–515. https://doi.org/10.1038/s41586-023-06145-x.

(6) Chen, Y. Nanofabrication by Electron Beam Lithography and Its Applications: A Review. *Microelectron. Eng.* **2015**, *135*, 57–72. https://doi.org/10.1016/j.mee.2015.02.042.

(7) Okazaki, S. High Resolution Optical Lithography or High Throughput Electron Beam Lithography: The Technical Struggle from the Micro to the Nano-Fabrication Evolution. *Microelectron. Eng.* **2015**, *133*, 23–35. https://doi.org/10.1016/j.mee.2014.11.015.

(8) Levinson, H. J. High-NA EUV Lithography: Current Status and Outlook for the Future. *Jpn. J. Appl. Phys.* **2022**, *61* (SD), SD0803. https://doi.org/10.35848/1347-4065/ac49fa.

(9) Chen, Y.; Xiong, S. Directed Self-Assembly of Block Copolymers for Sub-10 Nm Fabrication. *Int. J. Extreme Manuf.* **2020**, *2* (3), 032006. https://doi.org/10.1088/2631-7990/aba3ae.

(10) Bates, F. S.; Fredrickson, G. H. Block Copolymers—Designer Soft Materials. *Phys. Today* **1999**, *52* (2), 32–38. https://doi.org/10.1063/1.882522.

(11) Pound-Lana, G.; Bézard, P.; Petit-Etienne, C.; Cavalaglio, S.; Cunge, G.; Cabannes-Boué, B.; Fleury, G.; Chevalier, X.; Zelsmann, M. Dry-Etching Processes for High-Aspect-Ratio Features with Sub-10 Nm Resolution High-χ Block Copolymers. *ACS Appl. Mater. Interfaces* **2021**, *13* (41), 49184–49193. https://doi.org/10.1021/acsami.1c13503.

(12) Chevalier, X.; Gomes Correia, C.; Pound-Lana, G.; Bézard, P.; Sérégé, M.; Petit-Etienne, C.; Gay, G.; Cunge, G.; Cabannes-Boué, B.; Nicolet, C.; Navarro, C.; Cayrefourcq, I.; Müller, M.;

Hadziioannou, G.; Iliopoulos, I.; Fleury, G.; Zelsmann, M. Lithographically Defined Cross-Linkable Top Coats for Nanomanufacturing with High-χ Block Copolymers. *ACS Appl. Mater. Interfaces* **2021**, *13* (9), 11224–11236. https://doi.org/10.1021/acsami.1c00694.

(13) Baumgarten, N.; Mumtaz, M.; Merino, D. H.; Solano, E.; Halila, S.; Bernard, J.; Drockenmuller, E.; Fleury, G.; Borsali, R. Interface Manipulations Using Cross-Linked Underlayers and Surface-Active Diblock Copolymers to Extend Morphological Diversity in High-χ Diblock Copolymer Thin Films. *ACS Appl. Mater. Interfaces* **2023**, *15* (19), 23736–23748. https://doi.org/10.1021/acsami.3c02247.

(14) Suh, H. S.; Kim, D. H.; Moni, P.; Xiong, S.; Ocola, L. E.; Zaluzec, N. J.; Gleason, K. K.; Nealey, P. F. Sub-10-Nm Patterning via Directed Self-Assembly of Block Copolymer Films with a Vapour-Phase Deposited Topcoat. *Nat. Nanotechnol.* **2017**, *12* (6), 575–581. https://doi.org/10.1038/nnano.2017.34.

(15) Chevalier, X.; Pound-Lana, G.; Gomes Correia, C.; Cavalaglio, S.; Cabannes-Boué, B.; Restagno, F.; Miquelard-Garnier, G.; Roland, S.; Navarro, C.; Fleury, G.; Zelsmann, M. Self-Organization and Dewetting Kinetics in Sub-10 Nm Diblock Copolymer Line/Space Lithography. *Nanotechnology* **2023**, *34* (17), 175602. https://doi.org/10.1088/1361-6528/acb49f.

(16) Feng, H.; Dolejsi, M.; Zhu, N.; Yim, S.; Loo, W.; Ma, P.; Zhou, C.; Craig, G. S. W.; Chen, W.; Wan, L.; Ruiz, R.; De Pablo, J. J.; Rowan, S. J.; Nealey, P. F. Optimized Design of Block Copolymers with Covarying Properties for Nanolithography. *Nat. Mater.* **2022**, *21* (12), 1426–1433. https://doi.org/10.1038/s41563-022-01392-1.

(17) Yang, G.-W.; Wu, G.-P.; Chen, X.; Xiong, S.; Arges, C. G.; Ji, S.; Nealey, P. F.; Lu, X.-B.; Darensbourg, D. J.; Xu, Z.-K. Directed Self-Assembly of Polystyrene- *b* -Poly(Propylene Carbonate) on Chemical Patterns via Thermal Annealing for Next Generation Lithography. *Nano Lett.* **2017**, *17* (2), 1233–1239. https://doi.org/10.1021/acs.nanolett.6b05059.

(18) Pang, Y.; Jin, X.; Huang, G.; Wan, L.; Ji, S. Directed Self-Assembly of Styrene-Methyl Acrylate Block Copolymers with Sub-7 Nm Features via Thermal Annealing. *Macromolecules* **2019**, *52* (8), 2987–2994. https://doi.org/10.1021/acs.macromol.9b00174.

(19) Yoshimura, Y.; Chandra, A.; Nabae, Y.; Hayakawa, T. Chemically Tailored High- χ Block Copolymers for Perpendicular Lamellae *via* Thermal Annealing. *Soft Matter* **2019**, *15* (17), 3497–3506. https://doi.org/10.1039/C9SM00128J.

(20) Oh, J.; Suh, H. S.; Ko, Y.; Nah, Y.; Lee, J.-C.; Yeom, B.; Char, K.; Ross, C. A.; Son, J. G. Universal Perpendicular Orientation of Block Copolymer Microdomains Using a Filtered Plasma. *Nat. Commun.* **2019**, *10* (1), 2912. https://doi.org/10.1038/s41467-019-10907-5.

(21) Durand, W. J.; Blachut, G.; Maher, M. J.; Sirard, S.; Tein, S.; Carlson, M. C.; Asano, Y.; Zhou, S. X.; Lane, A. P.; Bates, C. M.; Ellison, C. J.; Willson, C. G. Design of High-χ Block Copolymers for Lithography. *J. Polym. Sci. Part Polym. Chem.* **2015**, *53* (2), 344–352. https://doi.org/10.1002/pola.27370.

(22) Park, S. -M.; Stoykovich, M. P.; Ruiz, R.; Zhang, Y.; Black, C. T.; Nealey, P. F. Directed Assembly of Lamellae- Forming Block Copolymers by Using Chemically and Topographically Patterned Substrates. *Adv. Mater.* **2007**, *19* (4), 607–611. https://doi.org/10.1002/adma.200601421.

(23) Gunkel, I. Directing Block Copolymer Self-Assembly on Patterned Substrates. *Small* **2018**, *14* (46), 1802872. https://doi.org/10.1002/smll.201802872.

(24) Xiong, S.; Wan, L.; Ishida, Y.; Chapuis, Y.-A.; Craig, G. S. W.; Ruiz, R.; Nealey, P. F. Directed Self-Assembly of Triblock Copolymer on Chemical Patterns for Sub-10-Nm Nanofabrication *via* Solvent Annealing. *ACS Nano* **2016**, *10* (8), 7855–7865. https://doi.org/10.1021/acsnano.6b03667.

(25) Legrain, A.; Fleury, G.; Mumtaz, M.; Navarro, C.; Arias-Zapata, J.; Chevalier, X.; Cayrefourcq, I.; Zelsmann, M. Straightforward Integration Flow of a Silicon-Containing Block Copolymer for Line–Space Patterning. *ACS Appl. Mater. Interfaces* **2017**, *9* (49), 43043–43050. https://doi.org/10.1021/acsami.7b12217.

(26) Doise, J.; Koh, J. H.; Kim, J. Y.; Zhu, Q.; Kinoshita, N.; Suh, H. S.; Delgadillo, P. R.; Vandenberghe, G.; Willson, C. G.; Ellison, C. J. Strategies for Increasing the Rate of Defect

Annihilation in the Directed Self-Assembly of High-χ Block Copolymers. *ACS Appl. Mater. Interfaces* **2019**, *11* (51), 48419–48427. https://doi.org/10.1021/acsami.9b17858.

(27) Lane, A. P.; Yang, X.; Maher, M. J.; Blachut, G.; Asano, Y.; Someya, Y.; Mallavarapu, A.; Sirard, S. M.; Ellison, C. J.; Willson, C. G. Directed Self-Assembly and Pattern Transfer of Five Nanometer Block Copolymer Lamellae. *ACS Nano* **2017**, *11* (8), 7656–7665. https://doi.org/10.1021/acsnano.7b02698.

(28) Aissou, K.; Kwon, W.; Mumtaz, M.; Antoine, S.; Maret, M.; Portale, G.; Fleury, G.; Hadziioannou, G. Archimedean Tilings and Hierarchical Lamellar Morphology Formed by Semicrystalline Miktoarm Star Terpolymer Thin Films. *ACS Nano* **2016**, *10* (4), 4055–4061. https://doi.org/10.1021/acsnano.5b06728.

(29) Ostrovskaya, L.; Perevertailo, V.; Ralchenko, V.; Dementjev, A.; Loginova, O. Wettability and Surface Energy of Oxidized and Hydrogen Plasma-Treated Diamond Films. *Diam. Relat. Mater.* **2002**, *11* (3–6), 845–850. https://doi.org/10.1016/S0925-9635(01)00636-7.

(30) Donnet, J. B.; Brendle, M.; Dhami, T. L.; Bahl, O. P. Plasma Treatment Effect on the Surface Energy of Carbon and Carbon Fibers. *Carbon* **1986**, *24* (6), 757–770. https://doi.org/10.1016/0008-6223(86)90186-7.

(31) Suni, T.; Henttinen, K.; Suni, I.; Makinen, J. Effects of Plasma Activation on Hydrophilic Bonding of Si and SiO2. *J. Electrochem. Soc.* **2002**, *149* (6), 348–351.

(32) Mertens, M.; Mohr, M.; Brühne, K.; Fecht, H. J.; Łojkowski, M.; Święszkowski, W.; Łojkowski, W. Patterned Hydrophobic and Hydrophilic Surfaces of Ultra-Smooth Nanocrystalline Diamond Layers. *Appl. Surf. Sci.* **2016**, *390*, 526–530. https://doi.org/10.1016/j.apsusc.2016.08.130.

(33) Constantoudis, V. Effects of Resist Sidewall Morphology on Line-Edge Roughness Reduction and Transfer during Etching: Is the Resist Sidewall after Development Isotropic or Anisotropic? *J. MicroNanolithography MEMS MOEMS* **2010**, *9* (4), 041209. https://doi.org/10.1117/1.3497601.

(34) Fouchier, M.; Pargon, E. HBr/O2 Plasma Treatment Followed by a Bake for Photoresist Linewidth Roughness Smoothing. *J. Appl. Phys.* **2014**, *115* (7), 074901. https://doi.org/10.1063/1.4865799.

(35) Owens, D. K.; Wendt, R. C. Estimation of the Surface Free Energy of Polymers. *J. Appl. Polym. Sci.* **1969**, *13* (8), 1741–1747. https://doi.org/10.1002/app.1969.070130815.

(36) Wu, S. Calculation of Interfacial Tension in Polymer Systems. *J. Polym. Sci. Part C Polym. Symp.* **1971**, *34* (1), 19–30. https://doi.org/10.1002/polc.5070340105.

(37) Turner, M. S. Equilibrium Properties of a Diblock Copolymer Lamellar Phase Confined between Flat Plates. *Phys. Rev. Lett.* **1992**, *69* (12), 1788–1791. https://doi.org/10.1103/PhysRevLett.69.1788.

(38) Walton, D. G.; Kellogg, G. J.; Mayes, A. M.; Lambooy, P.; Russell, T. P. A Free Energy Model for Confined Diblock Copolymers. *Macromolecules* **1994**, *27* (21), 6225–6228. https://doi.org/10.1021/ma00099a045.

(39) Stein, G. E.; Liddle, J. A.; Aquila, A. L.; Gullikson, E. M. Measuring the Structure of Epitaxially Assembled Block Copolymer Domains with Soft X-Ray Diffraction. *Macromolecules* **2010**, *43* (1), 433–441. https://doi.org/10.1021/ma901914b.

(40) Bates, C. M.; Seshimo, T.; Maher, M. J.; Durand, W. J.; Cushen, J. D.; Dean, L. M.; Blachut, G.; Ellison, C. J.; Willson, C. G. Polarity-Switching Top Coats Enable Orientation of Sub–10-Nm Block Copolymer Domains. *Science* **2012**, *338* (6108), 775–779. https://doi.org/10.1126/science.1226046.

(41) Keen, I.; Cheng, H.-H.; Yu, A.; Jack, K. S.; Younkin, T. R.; Leeson, M. J.; Whittaker, A. K.; Blakey, I. Behavior of Lamellar Forming Block Copolymers under Nanoconfinement: Implications for Topography Directed Self-Assembly of Sub-10 Nm Structures. *Macromolecules* **2014**, *47* (1), 276–283. https://doi.org/10.1021/ma4019735.

(42) Giammaria, T. J.; Gharbi, A.; Paquet, A.; Nealey, P.; Tiron, R. Resist-Free Directed Self-Assembly Chemo-Epitaxy Approach for Line / Space Patterning. **2020**.

(43) Wertheimer, M. R.; Fozza, A. C.; Holländer, A. Industrial Processing of Polymers by Low-Pressure Plasmas: The Role of VUV Radiation. *Nucl. Instrum. Methods Phys. Res. Sect. B Beam Interact. Mater. At.* **1999**, *151* (1–4), 65–75. https://doi.org/10.1016/S0168-583X(99)00073-7.

(44) Fantz, U.; Briefi, S.; Rauner, D.; Wünderlich, D. Quantification of the VUV Radiation in Low Pressure Hydrogen and Nitrogen Plasmas. *Plasma Sources Sci. Technol.* **2016**, *25* (4), 045006. https://doi.org/10.1088/0963-0252/25/4/045006.

(45) Khorasaninejad, M.; Chen, W. T.; Devlin, R. C.; Oh, J.; Zhu, A. Y.; Capasso, F. Metalenses at Visible Wavelengths: Diffraction-Limited Focusing and Subwavelength Resolution Imaging. *Science* **2016**, *352* (6290), 1190–1194. https://doi.org/10.1126/science.aaf6644.

(46) Genevet, P.; Capasso, F.; Aieta, F.; Khorasaninejad, M.; Devlin, R. Recent Advances in Planar Optics: From Plasmonic to Dielectric Metasurfaces. *Optica* **2017**, *4* (1), 139. https://doi.org/10.1364/OPTICA.4.000139.

(47) Jin, H. M.; Kim, J. Y.; Heo, M.; Jeong, S.-J.; Kim, B. H.; Cha, S. K.; Han, K. H.; Kim, J. H.; Yang, G. G.; Shin, J.; Kim, S. O. Ultralarge Area Sub-10 Nm Plasmonic Nanogap Array by Block Copolymer Self-Assembly for Reliable High-Sensitivity SERS. *ACS Appl. Mater. Interfaces* **2018**, *10* (51), 44660–44667. https://doi.org/10.1021/acsami.8b17325.

(48) Nugroho, F. A. A.; Albinsson, D.; Antosiewicz, T. J.; Langhammer, C. Plasmonic Metasurface for Spatially Resolved Optical Sensing in Three Dimensions. *ACS Nano* **2020**, *14* (2), 2345–2353. https://doi.org/10.1021/acsnano.9b09508.

(49) Nugroho, F. A. A.; Bai, P.; Darmadi, I.; Castellanos, G. W.; Fritzsche, J.; Langhammer, C.; Gómez Rivas, J.; Baldi, A. Inverse Designed Plasmonic Metasurface with Parts per Billion Optical Hydrogen Detection. *Nat. Commun.* **2022**, *13* (1), 5737. https://doi.org/10.1038/s41467-022-33466-8.